

1-9-2012

Investigation of the Interfacial Tension of Complex Coacervates Using Field-Theoretic Simulations

Robert A. Riggleman

University of Pennsylvania, rrig@seas.upenn.edu

Rajeev Kumar

Oak Ridge National Laboratory

Glenn H. Fredrickson

University of California - Santa Barbara

Riggleman, R., Kumar, R., and Fredrickson, G. (2012). *Journal of Chemical Physics*. Volume 136, Issue 2, 024903. <http://dx.doi.org/10.1063/1.3674305>

© 2012 American Institute of Physics. This article may be downloaded for personal use only. Any other use requires prior permission of the author and the American Institute of Physics.

The following article appeared in the *Journal of Chemical Physics* and may be found at R. A. Riggleman, R. Kumar, and G. Fredrickson, *J. Chem. Phys.* 136, 024903 (2012).

This paper is posted at ScholarlyCommons. http://repository.upenn.edu/cbe_papers/154

For more information, please contact repository@pobox.upenn.edu.

Investigation of the interfacial tension of complex coacervates using field-theoretic simulations

Robert A. Riggleman,¹ Rajeev Kumar,² and Glenn H. Fredrickson^{3,a)}

¹*Department of Chemical and Biomolecular Engineering, University of Pennsylvania, Philadelphia, Pennsylvania 19104, USA*

²*National Center for Computational Science, Oak Ridge National Laboratory, Oak Ridge, Tennessee 37831, USA*

³*Department of Chemical Engineering, Materials Department, and Materials Research Laboratory, University of California, Santa Barbara, California 93106, USA*

(Received 12 August 2011; accepted 12 December 2011; published online 9 January 2012)

Complex coacervation, a liquid-liquid phase separation that occurs when two oppositely charged polyelectrolytes are mixed in a solution, has the potential to be exploited for many emerging applications including wet adhesives and drug delivery vehicles. The ultra-low interfacial tension of coacervate systems against water is critical for such applications, and it would be advantageous if molecular models could be used to characterize how various system properties (e.g., salt concentration) affect the interfacial tension. In this article we use field-theoretic simulations to characterize the interfacial tension between a complex coacervate and its supernatant. After demonstrating that our model is free of ultraviolet divergences (calculated properties converge as the collocation grid is refined), we develop two methods for calculating the interfacial tension from field-theoretic simulations. One method relies on the mechanical interpretation of the interfacial tension as the interfacial pressure, and the second method estimates the change in free energy as the area between the two phases is changed. These are the first calculations of the interfacial tension from full field-theoretic simulation of which we are aware, and both the magnitude and scaling behaviors of our calculated interfacial tension agree with recent experiments. © 2012 American Institute of Physics. [doi:10.1063/1.3674305]

I. INTRODUCTION

A variety of mature and emerging technologies depend critically on the association of oppositely charged polymers or particles. Such association can take the form of layer-by-layer assembly of polymers on a charged substrate,^{1,2} or it could involve charge complexation in solution.^{3–5} Examples of emerging technologies that rely on these and related phenomena include wet adhesives for medical, construction, consumer, and military use,^{6,7} advanced biosensors, drug and gene delivery vehicles,^{8–10} and responsive and switchable surfaces.^{11,12} When the association takes place in solution, depending on the strength of the polyelectrolyte and the solvent conditions, the resulting polyelectrolyte complex can either be a solid precipitate or a polyelectrolyte-rich liquid phase termed a “complex coacervate.” Many of the applications exploiting complex coacervation that are currently under exploration depend critically on the interfacial properties of the coacervate phase with its supernatant, notably the ultra-low interfacial tension, yet the characterization of the interfacial properties of these systems has been limited.^{5,13}

It would be advantageous to employ modeling techniques to investigate the interfacial properties of coacervate systems, but it is a significant challenge to simulate such phases; accurate descriptions of the coacervate phase must take into account both the long-range electrostatic effects as well as

maintain the short-range connectivity of the polymer chains. Due to the long relaxation times inherent in polymers and the expense of incorporating electrostatic interactions using Coulomb’s law, particle-based simulations of the association of oppositely charged polyelectrolytes has been limited to relatively small systems.

An alternative approach to particle-based models is to use polymer field theory. Complex coacervation is a phase behavior that is driven by electrostatic correlations, and this has important consequences if one chooses to adopt a field-theoretic approach to the study of coacervation. Fluctuation/correlation effects are completely ignored in the commonly-employed self-consistent field theory (SCFT), and this means that SCFT is unable to capture complex coacervation. One can include field fluctuations by using the random-phase approximation (RPA), which incorporates fluctuations and electrostatic correlations at the Gaussian level.^{14–18} The RPA has also recently been used to explore the effects of chain stiffness on complex coacervation,¹⁹ showing that rod-like charged polymers can form a variety of phases, including various nematics in addition to coacervate phases. The phase envelope between an isotropic coacervate phase is much smaller for the rod-like polymers than for fully flexible polymers, indicating that chain stiffness can play a significant role in coacervation.

Several recent developments have made “field-theoretic simulations” (FTS) tractable,^{20,21} where the full fluctuations of the fields are taken into account. Recently, such an approach has been used to study complex coacervation.^{22,23} The

^{a)}Electronic mail: ghf@mrl.ucsb.edu.

phase diagram estimated from RPA was compared to the diagram calculated on the full FTS treatment, and it was shown that in the limit of high polymer concentrations, RPA does a satisfactory job of capturing the fluctuation effects and predicts a qualitatively accurate phase diagram. However, the RPA approach becomes inaccurate for systems with a high charge density, because it overestimates the charge correlations.

These previous studies demonstrate the promise of using field-theoretic approaches to describe coacervation. One challenge of adopting the field-theoretic approach is that it is a relatively new class of simulation, and therefore the techniques to calculate important material properties (e.g., the interfacial tension) have not yet been developed. In this study, we extend the previous FTS of complex coacervation^{22,23} by characterizing the interfacial properties between the coacervate and the solvent. Density profiles are calculated, and we adapt two techniques from the literature on particle-based simulations to calculate the interfacial tension from field-theoretic simulations. The two techniques differ considerably in their approach, and the interfacial tensions calculated from each technique agree with each other to within our uncertainty. We use our simulations to explore various scaling relationships between the interfacial tension and various system parameters (e.g., salt concentration and polymer charge density).

The rest of this article is organized as follows. In Sec. II, we describe our field-theoretic model in detail, our simulation techniques, and the two methods for calculating the interfacial tension. In Sec. III, we summarize our results for the density profiles, phase diagrams, and interfacial tension trends as we vary different system parameters. Sec. IV discusses our results in the context of different levels of theory and discusses the various scaling relationships. Finally, Sec. V summarizes our work.

II. THEORY AND METHODS

A. Polyelectrolyte model

The model considered in this work is similar to that considered in previous field-theoretic studies of polyelectrolyte systems exhibiting complex coacervation^{22,23} with some modifications. For completeness and to highlight some of the differences between our field-theoretic model and previous incarnations of the model, we will recount the model in detail. Our systems consist of flexible polycations and polyanions as well as small ions (counterions and salt). We model our polymer molecules as continuous Gaussian chains with a chain length of N and a uniformly distributed charge density along their backbone; there are n_+ polycations and n_- polyanions. The valency of each charge on the polycations is given by Z ($-Z$ for the polyanions), and the linear charge densities of the polycations and polyanions are given by β_+ and β_- , respectively. Such a homogeneous charge density along the polymer backbone is valid at relatively low charge densities, but for strongly-charged polymers, the discrete nature of the charges is important and models with both discrete charges and harsh repulsive (hard-core) short-ranged interactions be-

come necessary.^{24,25} In addition to the polymer chains, there are n_{s+} salt cations with a valency of Z_{s+} and n_{s-} salt anions with a valency of Z_{s-} . The small ions, both counterions and salt species, are modeled as point particles.

Many field-theoretic models possess so-called ultraviolet divergences (UV divergences); their properties can depend strongly on the underlying grid spacing used to solve the field theory equations, and certain properties diverge as the underlying grid is refined. Such divergences do not show up at the mean-field limit, and they are avoided for cases where SCFT is sufficient. The divergences arise due to infinite contact potentials such as the commonly-used Edwards delta function potential²⁶ or, in the case of charged systems like those considered here, the Coulomb potential.^{26–28} For calculations going beyond the mean-field approximation, these divergent terms are usually managed by either ignoring the divergent terms, applying a cut-off to the potential, or subtracting out a known reference state. In a recent important study of simple (non-polymeric) electrolyte solutions, Wang demonstrated that by distributing the charges for each small ion over a small volume (as opposed to the typical point charge model), he could derive a field-theoretic model for electrolytes that is free of UV divergences.²⁷ We adopt this approach to both the electrostatic interactions and the short-range excluded volume interactions in our model by distributing the mass and the charge of both polymer segments and small ions over a small volume. This effectively makes the potentials go smoothly to finite values at small distances.

For our polymer species we consider both the mass and the charge to have a Gaussian distribution about a central point, and the small ions that are treated are assumed to be massless/volumeless particles carrying a charge that has a Gaussian spatial distribution. Treating the small ions as massless/volumeless particles, we can write the density of our polycations and polyanions as

$$\hat{\rho}_{\pm}(\mathbf{r}) = N \sum_j^{n_{\pm}} \int_0^1 ds \Gamma[\mathbf{r} - \mathbf{r}_j(s)], \quad (1)$$

where s is the position along the j th polymer contour, and

$$\Gamma(\mathbf{r} - \mathbf{r}') = \left(\frac{1}{2\pi^2 a^2} \right)^{3/2} e^{-|\mathbf{r} - \mathbf{r}'|^2 / 2a^2} \quad (2)$$

is a normalized Gaussian function that approaches a delta function as $a \rightarrow 0$. The parameter a controls the breadth of the distribution of mass and charge; we choose a to be equal to the polymer statistical segment size, as we expect the mass and charge inside a statistical segment to be distributed over a length comparable to a .

The polymer chains are modeled as continuous Gaussian chains with a harmonic bond-stretching potential

$$\beta U_0 = \frac{3}{2a^2} \sum_{j=1}^{n_{\pm}} \int_0^1 ds \left| \frac{d\mathbf{r}_j(s)}{ds} \right|^2. \quad (3)$$

Here, a is the size of a statistical segment of the polymers, $\beta = 1/k_B T$, and s is the position along the contour of the polymer chain. The polymer segments interact with a

short-ranged, purely repulsive excluded volume potential given by

$$\beta U_1 = \frac{u_0}{2} \int d\mathbf{r} [\hat{\rho}_P(\mathbf{r})]^2. \quad (4)$$

The excluded volume parameter u_0 has units of volume and controls the strength of the repulsive interaction. The electrostatic interactions are taken through Coulomb's law

$$\beta U_2 = \frac{1}{2} \int d\mathbf{r} \int d\mathbf{r}' \hat{\rho}_c(\mathbf{r}) \frac{l_B}{|\mathbf{r} - \mathbf{r}'|} \hat{\rho}_c(\mathbf{r}'), \quad (5)$$

where $l_B = \beta e^2/\epsilon$ is the Bjerrum length, the dielectric constant of the medium (taken to be uniform) is ϵ , and e is the fundamental unit of charge. The Bjerrum length is the length scale on which the energy of the electrostatic interaction between two elementary charges is $k_B T$ in a given dielectric medium. $\hat{\rho}_c(\mathbf{r})$ is the total charge density given by

$$\hat{\rho}_c(\mathbf{r}) = Z\beta_+ \hat{\rho}_+(\mathbf{r}) - Z\beta_- \hat{\rho}_-(\mathbf{r}) + Z_{s+} \hat{\rho}_{s+}(\mathbf{r}) + Z_{s-} \hat{\rho}_{s-}(\mathbf{r}). \quad (6)$$

Taken together, we can write the partition function for our system in the canonical ensemble as

$$\mathcal{Z} = \frac{Z_0}{n_+! n_-! n_{s+}! n_{s-}!} \times \int \mathcal{D}\mathbf{r}^{n_P} \int d\mathbf{r}^{n_s} \exp[-\beta U_0 - \beta U_1 - \beta U_2], \quad (7)$$

where $n_P = n_+ + n_-$ is the total number of polymer chains, Z_0 contains the thermal de Broglie wavelengths and the self-interaction terms, $\int \mathcal{D}\mathbf{r}$ represents the path integral over the polymer contours, and $n_s = n_{s+} + n_{s-}$ is the total number of small ions. It is assumed that the salt ions and the counterions are indistinguishable. We are now in a position to convert our particle model into a field-based theory through the usual Hubbard-Stratonovich transformation,²⁸ resulting in a field-based partition function:

$$\mathcal{Z} = \frac{Z_0 V^{n_P+n_s}}{n_+! n_-! n_{s+}! n_{s-}! \Omega_0 \Psi_0} \times \int \mathcal{D}w \int \mathcal{D}\psi \exp(-H[w, \psi]). \quad (8)$$

$H[w, \psi]$ is the effective Hamiltonian for our system given in dimensionless form as

$$\begin{aligned} H[w, \psi] = & \frac{1}{2B} \int d\mathbf{r} w(\mathbf{r})^2 + \frac{1}{2E} \int d\mathbf{r} |\nabla \psi(\mathbf{r})|^2 \\ & - C_+ V \ln Q_+[\omega_+] - C_- V \ln Q_-[\omega_-] \\ & - C_{s+} V \ln Q_{s+} \left[\frac{iZ_{s+}}{ZN} (\Gamma * \psi) \right] \\ & - C_{s-} V \ln Q_{s-} \left[\frac{iZ_{s-}}{ZN} (\Gamma * \psi) \right]. \end{aligned} \quad (9)$$

All coordinates \mathbf{r} are scaled by the unperturbed polymer radius of gyration, $R_g = a^* \sqrt{N/6}$. The asterisk (*) is a shorthand for the convolution integral, Ω_0 and Ψ_0 are normalization constants that arise from the Gaussian integrals employed in the Hubbard-Stratonovich transformation, and

the fields $\omega_{\pm}(\mathbf{r})$ are the potential fields experienced by the polyelectrolytes, given by

$$w_{\pm}(\mathbf{r}) = i [w(\mathbf{r}) \pm \beta_{\pm} \psi(\mathbf{r})], \quad (10)$$

$$\omega_{\pm}(\mathbf{r}) = (\Gamma * w_{\pm})(\mathbf{r}). \quad (11)$$

The dimensionless parameters are given by

$$B = \frac{u_0 N^2}{R_g^3}, \quad E = \frac{4\pi l_B N^2 Z^2}{R_g}, \quad C_K = \frac{n_K R_g^3}{V}. \quad (12)$$

B is the dimensionless excluded volume parameter, E is a dimensionless Bjerrum length, and C_K is a dimensionless concentration of species K .

The polymer partition functions $Q_{\pm}[\omega_{\pm}]$ are calculated by integrating the single chain propagators $q_{\pm}(\mathbf{r}, s; [\omega_{\pm}])$ as

$$Q_{\pm}[\omega_{\pm}] = \frac{1}{V} \int d\mathbf{r} q_{\pm}(\mathbf{r}, 1; [\omega_{\pm}]) \quad (13)$$

The propagators are calculated as the solution to the modified diffusion equation

$$\frac{\partial q_{\pm}}{\partial s} = \nabla^2 q_{\pm} - \omega_{\pm} q_{\pm} \quad (14)$$

subject to the initial condition $q_{\pm}(\mathbf{r}, 0) = 1$. The polymer density operators can be calculated from the chain propagators as

$$\tilde{\rho}_{\pm}(\mathbf{r}) = \frac{n_{\pm} N}{Q_{\pm} V} \int_0^1 ds q(\mathbf{r}, s; [\omega_{\pm}]) q(\mathbf{r}, 1-s; [\omega_{\pm}]). \quad (15)$$

The small ion partition functions are calculated as

$$Q_{s\pm}[\psi] = \frac{1}{V} \int d\mathbf{r} \exp \left[-\frac{iZ_{s\pm}}{ZN} \psi(\mathbf{r}) \right], \quad (16)$$

and the small ion density operators are

$$\rho_{s\pm}[\psi] = \frac{n_{s\pm}}{V Q_{s\pm}} \exp \left[-\frac{iZ_{s\pm}}{ZN} \psi(\mathbf{r}) \right]. \quad (17)$$

B. Pressure operator

We calculate the pressure tensor in our simulations by adopting the convention that the pressure $P_{\alpha\beta} = -\tau_{\alpha\beta}$, where $\tau_{\alpha\beta}$ is the stress tensor,²⁹ defined as

$$\tau_{\alpha\beta} = \frac{1}{V_0} \left(\frac{\partial F}{\partial \epsilon_{\alpha\beta}} \right). \quad (18)$$

The shape of our simulation box is described by a tensor \mathbf{h} ; for a rectangular simulation box, \mathbf{h} is diagonal with the box lengths in each direction along the diagonal. The strain tensor ϵ can be written in terms of \mathbf{h} as³⁰

$$\epsilon_{\alpha\beta} = \frac{1}{2} \left[\sum_{\gamma, \eta} (h_{\alpha\gamma}^0)^{-1} G_{\gamma\eta} (h_{\eta\beta}^0)^{-1} - \delta_{\alpha\beta} \right], \quad (19)$$

where the superscript 0 implies a reference simulation box shape, $G_{\alpha\beta}$ is the metric tensor defined as $\mathbf{G} = \mathbf{h}^T \cdot \mathbf{h}$, and $\delta_{\alpha\beta}$ is the Kronecker delta function. Using $\beta F = -\ln \mathcal{Z}$, inserting Eq. (8) for the partition function, and noting that \mathbf{h} is

diagonal for a rectangular simulation box, the diagonal components of the pressure tensor can be calculated as

$$P_{\alpha\alpha} = \frac{k_B T L_\alpha}{V} \left[\frac{n_T}{L_\alpha} - \frac{M}{L_\alpha} + \frac{1}{L_\alpha} \sum_{\mathbf{k}} \frac{k_\alpha^2}{k^2} - \left\langle \frac{\partial H}{\partial L_\alpha} \right\rangle \right], \quad (20)$$

where the angular brackets indicate an ensemble average over field configurations, and the sum over \mathbf{k} is taken over all wavevectors consistent with the grid on which the field theory is evaluated. Inside the square brackets in Eq. (20), the first term is the ideal gas contribution, and the second and third terms arise from the derivatives of Ω_0 and Ψ_0 .

The final step is to obtain the derivative of $H[w, \psi]$ with respect to the box dimensions L_α ; this can be done via explicit differentiation and is detailed in Appendix A. The final expression is

$$\begin{aligned} \left(\frac{\partial H}{\partial L_\alpha} \right) = & \frac{1}{2BL_\alpha} \int d\mathbf{r} w(\mathbf{r})^2 - \frac{1}{EL_\alpha} \\ & \times \int d\mathbf{r} \left[(\nabla_\alpha \psi)^2 - \frac{1}{2} |\nabla \psi|^2 \right] \\ & + \frac{2n_+}{VQ_+L_\alpha} \int d\mathbf{r} \int ds q(\mathbf{r}, s; [\omega_+]) \\ & \times \nabla_\alpha^2 q(\mathbf{r}, 1-s; [\omega_+]) \\ & - \frac{a^2}{NL_\alpha} \int d\mathbf{r} \tilde{\rho}_+(\mathbf{r}) \cdot (\Gamma * \nabla_\alpha^2 w_+)(\mathbf{r}) \\ & + \frac{2n_-}{VQ_-L_\alpha} \int d\mathbf{r} \int ds q(\mathbf{r}, s; [\omega_-]) \\ & \times \nabla_\alpha^2 q(\mathbf{r}, 1-s; [\omega_-]) \\ & - \frac{a^2}{NL_\alpha} \int d\mathbf{r} \tilde{\rho}_-(\mathbf{r}) \cdot (\Gamma * \nabla_\alpha^2 w_-)(\mathbf{r}) \\ & - \frac{iZ_+a^2}{ZNL_\alpha} \int d\mathbf{r} \tilde{\rho}_{s+}(\mathbf{r}) \cdot (\Gamma * \nabla_\alpha^2 \psi)(\mathbf{r}) \\ & - \frac{iZ_-a^2}{ZNL_\alpha} \int d\mathbf{r} \tilde{\rho}_{s-}(\mathbf{r}) \cdot (\Gamma * \nabla_\alpha^2 \psi)(\mathbf{r}). \quad (21) \end{aligned}$$

C. Calculation of the interfacial tension

To date the interfacial tension γ has not been calculated from a field-theoretic simulation. In particle-based simulations, approaches for calculating γ generally fall into two categories: those that rely on a thermodynamic interpretation of the interfacial tension and those that rely on a mechanical interpretation. Here we will follow both approaches. The mechanical definition of the interfacial tension in terms of the pressure profile is given by³¹

$$\gamma = \frac{1}{2} \int_0^{L_z} dz [P_N(z) - P_T(z)]. \quad (22)$$

Here $P_N(z)$ and $P_T(z)$ are the components of the pressure tensor that are normal and tangential to the interface, respectively, and the prefactor of 1/2 arises due to the presence of two interfaces between the coexisting phases in a canonical ensemble simulation with periodic boundary conditions. For

reasons of mechanical stability, the normal component $P_N(z)$ is expected to be uniform throughout, while $P_T(z)$ will contain a large, negative peak at the interface due to the tension in the plane. Even though there is substantial debate about the precise form of the local pressure $\mathbf{P}(\mathbf{r})$,^{32–35} this formula has been successfully applied to a wide variety of systems (e.g., Refs. 35 and 36). One can also take the integrated form of Eq. (22) to obtain a interfacial tension estimate that only depends on the components of the volume-averaged (global) pressure tensor³⁷ as

$$\gamma = \frac{1}{2} L_z \left[P_{zz} - \frac{1}{2} (P_{xx} + P_{yy}) \right]. \quad (23)$$

Here we have made the substitutions $P_N = P_{zz}$ and $P_T = \frac{1}{2}(P_{xx} + P_{yy})$, which are specific to the geometry of our simulation box, and each can be calculated using Eqs. (20) and (21).

The thermodynamic definition of the interfacial tension is

$$\gamma = \left(\frac{\partial F}{\partial A} \right)_{NVT}, \quad (24)$$

and a thermodynamic estimate of the interfacial tension relies on calculating the change in the free energy of a system as the interfacial area between two phases is changed by a small amount. Several techniques exist to calculate the interfacial tension in particle-based simulations using the thermodynamic definition, many of which were recently compared in an article by Errington and Kofke.³⁸ However, free energy methods are only just emerging for field-theoretic simulations,³⁹ and many of the approaches used in particle simulations cannot be easily applied. In complex Langevin sampling, individual configurations are taken from a distribution that only corresponds to the equilibrium distribution given in Eq. (8) after taking an ensemble average. This precludes the use of many flat histogram techniques that are based on probabilities associated with individual configurations. The sole free energy technique that has been developed for complex Langevin simulations is thermodynamic integration.³⁹

For our thermodynamic estimate of γ , we have adapted Bennett's method^{38,40,41} to field-theoretic simulations. The derivation of the method as applied to a field theory is given in Appendix B. For interfacial tension calculations, we discretize Eq. (24) and calculate the free energy change ΔF resulting from a small change in the interfacial area of our system $\Delta A = A_1 - A_0$. Bennett's method requires performing two independent simulations with interfacial area A_0 and A_1 . During the course of the simulation with A_0 the system is perturbed such that it has area A_1 without changing the field values, and the change in the system Hamiltonian $\Delta\mathcal{H}_{01}$ is calculated. The simulation then resumes with the original interfacial area A_0 . Similarly, a perturbation is performed on the simulation with interfacial area A_1 such that it has A_0 , and $\Delta\mathcal{H}_{10}$ is calculated. The procedure is repeated to accumulate statistics which are accumulated on $\Delta\mathcal{H}_{01}$ and $\Delta\mathcal{H}_{10}$, and we numerically solve:

$$\langle f(-\Delta\mathcal{H}_{01} + C) \rangle_0 = \langle f(-\Delta\mathcal{H}_{10} - C) \rangle_1, \quad (25)$$

for the parameter C , where $f(x)$ is the Fermi function

$$f(x) = \frac{1}{1 + \exp(x)}. \quad (26)$$

The free energy change is calculated as

$$\beta \Delta F = -\ln \left[\frac{\langle f(-\Delta \mathcal{H}_{01} + C) \rangle_0}{\langle f(-\Delta \mathcal{H}_{10} - C) \rangle_1} \right] + C \approx C, \quad (27)$$

and we finally obtain the interfacial tension as $\gamma = \frac{1}{2} \Delta F / \Delta A$. As in the mechanical definition of the interfacial tension, the prefactor of $\frac{1}{2}$ arises because our simulations in cells with periodic boundary conditions contain two interfaces.

D. Gaussian fluctuations

Because coacervation is driven by the strong correlations present in charged systems, neglecting all fluctuations and employing the mean-field approximation results in a theory that is unable to describe coacervation. Such fluctuation effects can be considered analytically using loop expansions of the free energy. Prior field-theoretic studies of coacervation have shown that retaining the fluctuations to Gaussian order captures a significant portion of the fluctuation effects; this is the “one-loop” or random phase approximation, which is a common approach in polymer field theory that can be used to incorporate fluctuation effects analytically. It is instructive to compare the RPA predictions to the results for our CL simulations sampling the fully fluctuating fields. For the symmetric case where $n_+ = n_- = n$, $\beta_+ = \beta_- = 1$, and no small ions $n_{s+} = n_{s-} = 0$, the RPA expression for the free energy is given by

$$\begin{aligned} \beta F = & \beta F_0 + \frac{1}{2} B C^2 V - 2n \ln V \\ & + \frac{V}{4\pi^2} \int_0^\infty dk k^2 [\ln(1 + B C \hat{g}_D(k) \hat{\Gamma}(k)^2) \\ & + \ln(1 + E C \hat{g}_D(k) \hat{\Gamma}(k)^2 / k^2)]. \end{aligned} \quad (28)$$

The $\hat{\cdot}$ symbol in the above equation denotes the Fourier transform of a function, k is the wave vector, and $\hat{g}_D(k)$ is the Debye function, expressed in Fourier space as

$$\hat{g}_D(k) = \frac{2}{k^4} (e^{-k^2} + k^2 - 1). \quad (29)$$

From this expression for βF , we can derive other thermodynamic functions such as the excess chemical potential,

$$\begin{aligned} \beta \mu_{ex} = & B C + \frac{V}{4\pi^2} \int_0^\infty dk k^2 \left[\frac{B \hat{g}_D(k) \hat{\Gamma}(k)^2}{1 + B C \hat{g}_D(k) \hat{\Gamma}(k)^2} \right. \\ & \left. + \frac{E \hat{g}_D(k) \hat{\Gamma}(k)^2}{k^2 + E C \hat{g}_D(k) \hat{\Gamma}(k)^2} \right], \end{aligned} \quad (30)$$

and the pressure

$$\begin{aligned} \beta R_g^3 P = & C + \frac{1}{2} B C^2 - \frac{1}{4\pi^2} \int_0^\infty dk k^2 \\ & \times \left[\ln(1 + B C \hat{g}_D(k) \hat{\Gamma}(k)^2) \right. \end{aligned}$$

$$\begin{aligned} & + \ln(1 + E C \hat{g}_D(k) \hat{\Gamma}(k)^2 / k^2) \\ & - \frac{B C \hat{g}_D(k) \hat{\Gamma}(k)^2}{1 + B C \hat{g}_D(k) \hat{\Gamma}(k)^2} \\ & \left. - \frac{E C \hat{g}_D(k) \hat{\Gamma}(k)^2}{k^2 + E C \hat{g}_D(k) \hat{\Gamma}(k)^2} \right]. \end{aligned} \quad (31)$$

It should be noted that the integrals in the above equations are UV-convergent because of the presence of Gaussian smearing functions, $\hat{\Gamma}(k)$.

E. Numerical methods

Our theory is evaluated in real space with periodic boundary conditions on a collocation grid, and the modified diffusion equation (Eq. (14)) is solved for $q_\pm(\mathbf{r}, s; [w_\pm])$ using a pseudo-spectral algorithm^{28,42,43} with the initial condition $q_\pm(\mathbf{r}, 0; [w_\pm]) = 1$. Due to the complex nature of our field theory and the inability of the mean-field approximation to capture complex coacervation, we sample our field configurations using complex Langevin (CL) sampling techniques.^{20,28,44,45} CL involves extending the functional integrals of the fields in our partition function \mathcal{Z} (Eq. (8)) over the *entire* complex plane and sampling field configurations using a Langevin dynamics scheme

$$\frac{\partial w}{\partial t} = -\lambda_w \left(\frac{\delta \mathcal{H}}{\delta w} \right) + \eta(\mathbf{r}, t), \quad (32)$$

where $\eta(\mathbf{r}, t)$ is a Gaussian-distributed, purely real random force acting on the field with the statistics

$$\langle \eta(\mathbf{r}, t) \rangle = 0, \quad (33)$$

$$\langle \eta(\mathbf{r}, t) \eta(\mathbf{r}', t') \rangle = 2\lambda_w \delta(\mathbf{r} - \mathbf{r}') \delta(t - t'). \quad (34)$$

To perform a CL simulation, Eq. (32) is discretized in t and iterated to evolve the field configurations $w(\mathbf{r})$ and $\psi(\mathbf{r})$ with $\lambda_w = \lambda_\psi = 0.025$ and time step $\delta t = 1$. To affect the time integration of Eq. (32), we employ the exponential time differencing algorithm of Ref. 46, which exhibits remarkable stability and accuracy even for relatively large time steps compared to other semi-implicit approaches.²¹ We emphasize that t does not represent a physical time variable, and the evolution of our fields according to Eq. (32) do not yield realistic dynamics of our system.

Unless otherwise noted, all calculations were performed in a simulation box of dimensions $L_x = L_y = 3R_g$, $L_z = 45R_g$, using numbers of grid points $N_x = N_y = 15$, and $N_z = 225$, and the polymer chains were discretized into $N_s = 81$ contour points. Each trajectory continued until average properties stopped changing to within 5%–10%, which typically required $\sim 5 \times 10^5$ time steps. All simulations are performed in triplicate and averaged over the three independent simulation trajectories, and the error bars are the standard error of the calculations amongst the three trajectories.

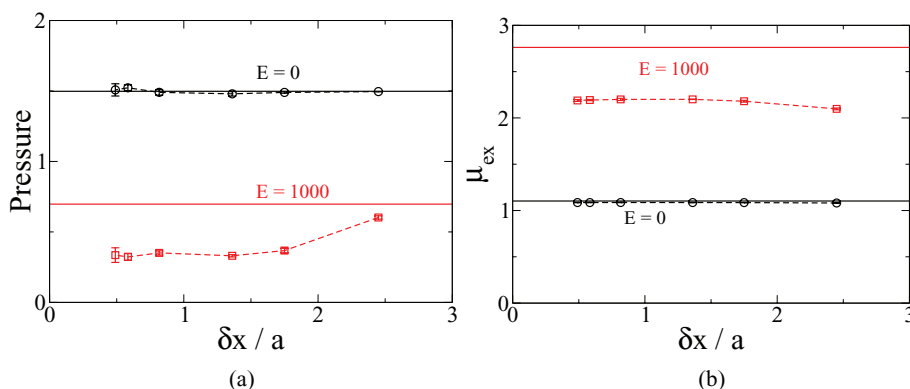


FIG. 1. UV convergence of the dimensionless pressure $\beta P R_g^3$ (a) and the excess chemical potential of the polycations (b) at $C_{\pm} = 0.5$, $B = 1.0$, and $C_{s\pm} = 0$; at these conditions, the system exists as a homogeneous phase. The x-axis in both cases is the grid spacing divided by the parameter a . Systems both with electrostatics ($E = 1000$ in red) and without electrostatic interactions ($E = 0$ in black) are shown. The solid horizontal lines show the RPA predictions for the model while the dashed lines show the results from the CL simulations that numerically sample the fully fluctuating fields. Each property was calculated in a cubic simulation box with periodic boundary conditions and $L_{\alpha} = 3.0R_g$.

III. RESULTS

A. UV convergence

We begin by demonstrating the UV convergence of our model through the inclusion of the Gaussian “smearing” functions $\Gamma(\mathbf{r} - \mathbf{r}')$ that distribute the mass and the charge over a small volume characterized by the parameter a . Figure 1 shows how two properties, the dimensionless pressure P and the excess chemical potential μ_{ex} change as we refine the collocation grid employed in our field-theoretic simulations for polymer solutions both with and without electrostatic interactions. Once the grid spacing δx becomes comparable to a ($\delta x \lesssim 1.7a$), the properties from the field-theoretic simulations cease changing as δx is refined, confirming that our model is UV-convergent. It is interesting to note that the UV-divergences are significantly weaker in the system without electrostatics ($E = 0$). RPA also does an excellent job of predicting μ_{ex} and P for the system without electrostatics at this polymer concentration, but we do not see quantitative agreement between RPA and the full field theory for the system with electrostatic interactions. All subsequent calculations were performed at grid spacings where $\delta x/a \leq 1.5$, ensuring UV-convergence of our results.

B. Density Profiles

Figure 2 plots the density profiles of the polymer and the small ions for the case where a symmetric salt is used (Fig. 2(a)) and where an asymmetric salt is employed (Fig. 2(b)) at the same polymer concentration $C_{\pm} = 1.5$ and electrostatic strength $E = 20000$. In both cases, the segregation is strong and all of the polymer is in the coacervate phase. The concentration of the small salt ions is slightly enriched in the coacervate phase, consistent with prior results obtained for rodlike polyelectrolytes using the RPA.¹⁹ For the asymmetric salts, the small cations carry a charge of $+2$ while the anions carry -1 . Although it appears in Fig. 2(b) that there is a small difference in the two profiles after they are scaled to lie on the same axis, the net charge throughout the system is zero. The reader should note that there are no harsh repulsive interactions in our model to saturate ion binding/bridging caused by multi-valent counterions. Thus, the example of Fig. 2(b) is a hypothetical, but illustrative case.

Another means for breaking the symmetry of the coacervate-forming systems is to change the amount of charge arising from one of the two polyelectrolyte components. This is explored in two ways: first, we decrease the linear charge

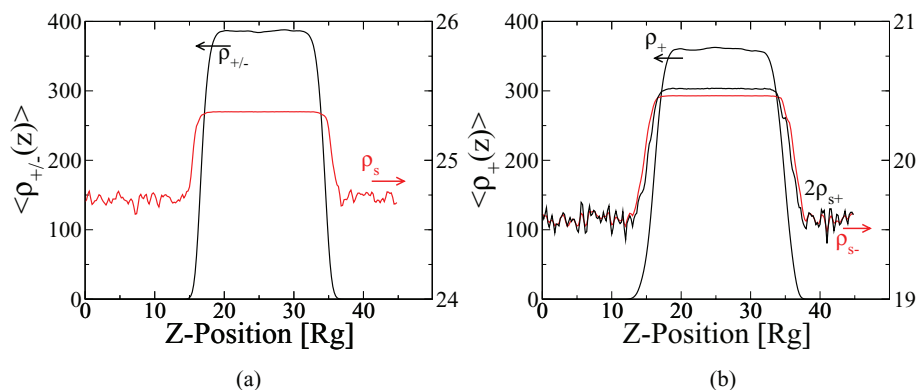


FIG. 2. Density profiles of the polymer (left axis) and the small ions (right axis) for a system with $E = 20000$, $B = 0.05$, and $C_{\pm} = 1.5$. a) The density profile for a case with symmetric salt ($Z_{s\pm} = \pm 1$) and $C_{s\pm} = 25$. The curves for the polycations and polyanions lie directly on top of each other; similarly, the profiles for the small cations and anions overlap. b) The density profiles for a system with an asymmetric salt with $Z_{s+} = 2$, $Z_{s-} = -1$, $C_{s+} = 10$, and $C_{s-} = 20$. The density profile for the small cations has been scaled so that it lies on the same y-axis as the anions.

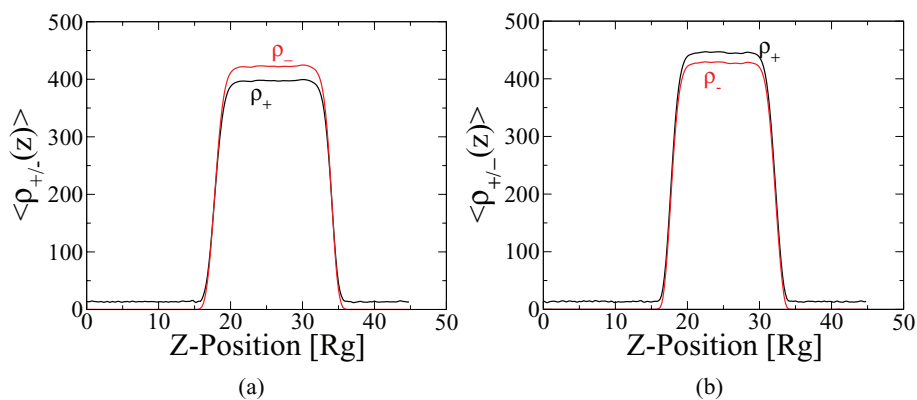


FIG. 3. Polymer chain concentration profiles of the polycations (ρ_+) and the polyanions (ρ_-) at $E = 20000$ and $B = 0.05$ for two cases where the charge arising from the two polyelectrolytes is asymmetric. (a) $C_+ = C_- = 1.5$, $\beta_+ = 1.0$, and $\beta_- = 0.9$. (b) $\beta_+ = \beta_- = 1.0$, $C_+ = 1.5$, and $C_- = 1.35$. In both cases, overall charge neutrality is maintained by adding $C_{s-} = 15$, and Z is fixed at ± 1 for both species.

density along the polymer backbone by setting $\beta_- = 0.9$ while keeping the concentration of the two polyelectrolytes equal, and second, we decrease the concentration of the polyanions to $C_- = 0.9C_+$ while keeping the linear charge densities of the two polymer species equal. In both cases, the net charge neutrality was maintained by adding an excess number of small anions ($C_{s-} = 15$). The plots of the resulting density profiles are shown in Fig. 3. Whether we break the symmetry by reducing the linear charge density or the concentration of polyanions, all of the polyanions segregate to the coacervate phase. Meanwhile, some of the polycations, which carry more charge than the polyanions, are forced into the solution phase. It is interesting that when the linear charge density is decreased, the concentration of the polyanions in the coacervate phase is *higher* than that of the polycations while the reverse is true when the concentration of the polyanions is decreased. In all cases, local charge neutrality is upheld.

C. Interfacial tension and phase behavior

Figure 4 demonstrates how the polycation concentration in the coacervate phase and the interfacial tension change

as the strength of the electrostatics (E) is changed. As E is decreased, the driving force for phase separation decreases, the polymer concentration in the coacervate phase decreases, and the interfacial tension between the coacervate and the solvent-rich supernatant phase decreases. Figure 4(b) compares the two methods for calculating the interfacial tension, and we find excellent agreement between the pressure tensor approach and Bennett's method; each point agrees within our uncertainty. The magnitudes of our interfacial tensions are also in good agreement with experimental values; our dimensionless interfacial tension γ is related to the interfacial tension in laboratory units (γ^*) through $\gamma = \beta\gamma^*R_g^2$. By taking $\beta = 1/k_B T$ at $T = 300$ K and $R_g^2 = Na^2/6$ with $a = 1.5$ nm, we find that $\gamma = 1$ corresponds to $\gamma^* \approx 100$ $\mu\text{N/m}$, in good agreement with recent experimental measurements.¹³

In Fig. 5(a) we plot the change in the polycation concentration in the coacervate phase as the excluded volume parameter B is increased compared to the binodal and spinodal phase boundaries calculated from RPA. Qualitatively, RPA does an excellent job of representing the full field theory, and the concentrations calculated from the field-theoretic simulations are approximately 50% higher than those predicted by

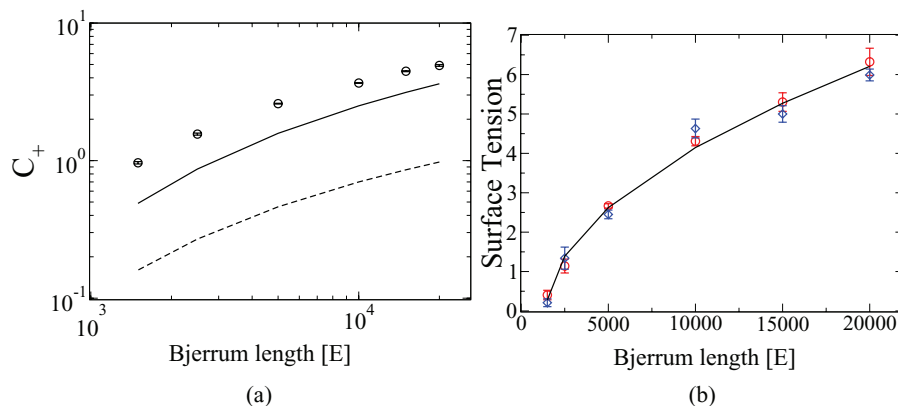


FIG. 4. (a) Polycation concentration in the coacervate phase and (b) interfacial tension as a function of the dimensionless Bjerrum length E . In (a), the circular points are the results of our CL simulations, and the solid and dashed lines are the binodal and spinodal predictions of the RPA, respectively. In (b), red circles are calculated using the pressure tensor method and the blue diamonds are calculated using Bennett's method; the solid line represents the $\gamma \propto (E - E_{cr})^{0.52}$, with $E_{cr} \approx 1490$. All calculations represented in these figures were with $B = 0.05$, $\beta_+ = \beta_- = 1$, $Z = \pm 1$, $C_{s\pm} = 0$, and the total polymer concentration was adjusted so that the coacervate phase occupied approximately half of the simulation box.

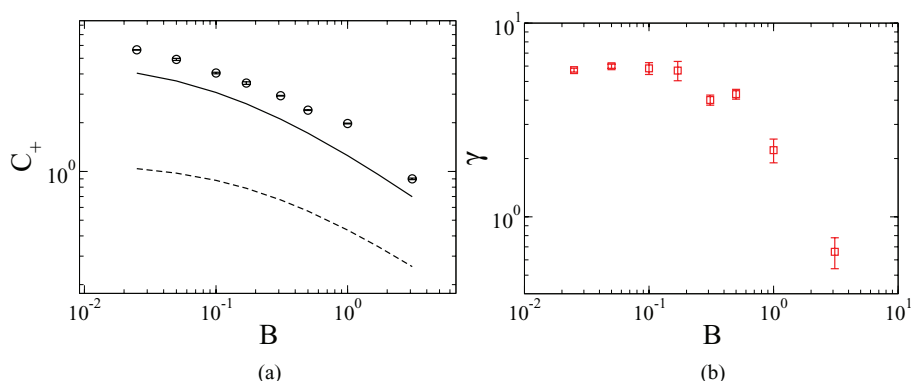


FIG. 5. Log-log plot of the polycation concentration in the coacervate phase (a) and the interfacial tension (b) as the excluded volume parameter B is increased. In (a), the solid and dashed lines represent the binodal and spinodal coexistence curves calculated using the RPA. The estimates of γ in (b) were obtained using Bennett's method. All calculations in these figures were performed with $E = 20000$, $\beta_+ = \beta_- = 1$, $Z = \pm 1$, $C_{s\pm} = 0$, and the total polymer concentration was adjusted so that the coacervate phase occupied approximately half of the simulation box.

the RPA binodal. Figure 5(b) shows how the interfacial tension decreases as the excluded volume parameter is increased, and the changes are relatively small, particularly for small B . As B increases and a critical point is approached, γ drops off sharply.

Figure 6 shows the influence of added salt on the polymer concentration in the coacervate and the interfacial tension between the supernatant and the coacervate. The range of salt concentration that is accessible is limited by the sizes of the systems that we can simulate; as we increase the salt concentration the electrostatics are screened, and both the concentration of the polymers in the coacervate phase and the interfacial tension decrease. This causes the coacervate phase to occupy more of our simulation box, and eventually the coacervate phase “sees” itself through the periodic boundaries. At this point, we either artificially observe a single phase or calculate inaccurate concentrations and interfacial tensions. Nevertheless, we are able to probe salt concentrations where the interfacial tension becomes relatively small.

IV. DISCUSSION

A. Interfacial tension calculations

We have developed two distinctly different approaches for calculating the interfacial tension from field-theoretic

simulations. One approach is based on a mechanical interpretation of interfacial tension where a line of tension maintains the interface between the two phases, and a second is based on the thermodynamic definition where we numerically estimate the partial derivative $\gamma = (\partial F / \partial A)_{NVT}$. For many conditions, the computational burden for each method is approximately the same. To obtain satisfactory statistics, the pressure tensor requires simulations that are approximately twice as long as Bennett's method. However, Bennett's method requires performing two separate simulations, and each estimate of $\Delta \mathcal{H}_{ij}$ in Bennett's method carries the same computational burden as an evaluation of the pressure tensor. A single evaluation of either the pressure tensor or $\Delta \mathcal{H}_{ij}$ requires the evaluation with the computational cost that scales $N_s M \log(M)$, where M is the total number of grid points. Bennett's method is more straightforward to implement, because it only requires perturbing the shape of the simulation box and calculating \mathcal{H} while the pressure tensor method requires deriving and evaluating the derivative given in Eqs. (20) and (21).

B. Scaling relationships

With the parameter space covered by C_s , B , and E , we are in a position to examine the scaling relationships between a variety of our system parameters and the calculated

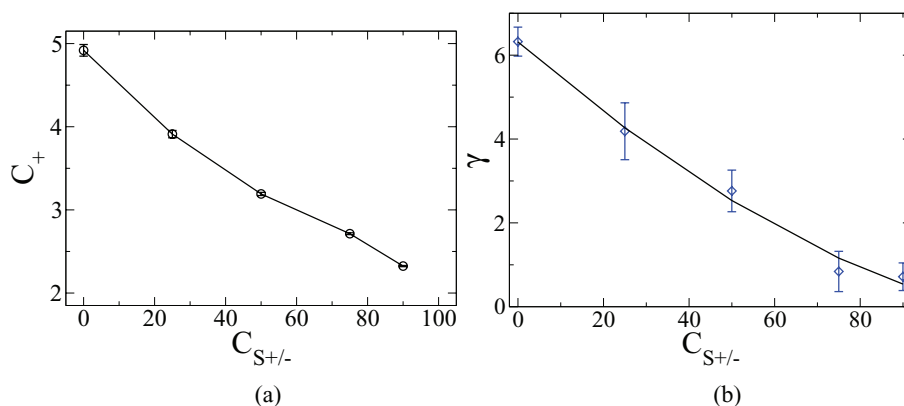


FIG. 6. (a) Changes in the polycation concentration in the coacervate phase and (b) the interfacial tension as the salt concentration is increased. In (a), the solid line is simply a guide to the eye, while in (b), the solid line represents the scaling $\gamma \propto (C_{s,crit} - C_s)^{3/2}$ with $C_{s,crit} \approx 110$. All calculations in these figures were performed with $E = 20000$, $B = 0.05$, $C = 1.5$, $\beta_{\pm} = 1$ and $Z = \pm 1$.

interfacial tension between the coacervate and supernatant phases. Spruijt and co-workers¹³ find that the interfacial tension of a coacervate comprised of strong polyelectrolytes scales with the concentration of added salt as $\gamma \propto (C_{s,crit} - C_s)^{3/2}$; they rationalize this scaling based on a mean-field argument with an effective χ parameter $\chi_{eff} = \chi + \frac{2\pi}{3} \frac{l_B \kappa^{-1} \sigma^2}{l^3}$, where κ^{-1} is the Debye screening length. As shown above in Fig. 6, we find a similar scaling in our simulations, although it is clear that the finite tension and the very existence of coacervation are intrinsically non-mean-field phenomena. We should note that careful experiments examining changes in the interfacial tension of phase-separated simple electrolytes where the two phases have a difference in dielectric constants have found that the interfacial tension has a non-monotonic dependence on salt concentration^{47,48} (the so-called “Jones-Ray effect”) whereby γ decreases at small salt concentrations before increasing at larger concentrations. This effect is not yet well-understood, but is believed to be due to differences in solvation effects of the salt ions in the two dielectric media.⁴⁹ Such effects are not incorporated into our field-theoretic model as we adopt a uniform dielectric; this remains an interesting area for future developments.

The previous work by Lee and co-workers²² found that the polymer concentration in the coacervate phase in the absence of salt scaled approximately as $C \propto B^{-0.64}$, where C is the concentration of polymer in the coacervate phase; in Fig. 5 above in our results from our RPA curves or the coexistence points measured from the CL simulations, we find that the change in C with B is weaker than the exponent observed by Lee *et al.* The RPA expressions employed by Lee *et al.* are in the concentrated limit of $BC \gg 1$, and this may account for those differences. It is interesting that the interfacial tension appears to plateau for small values of B and drops off sharply as the critical point is approached.

From a Widom-type scaling picture, one may expect that the interfacial tension should scale as $\gamma \propto k_B T \xi^2$, where $\xi \sim R_g (EC)^{-1/4}$ is the electrostatic screening length that emerges from the RPA for polyelectrolytes in the concentrated, no-salt limit. This scaling is tested in Fig. 7, and it appears to hold for all but the smallest value of (CE) , which departs significantly from this trend. A similar scaling relationship has been derived in θ -solvent conditions using scaling arguments⁵⁰ and RPA⁵¹, where $\gamma \propto E^{4/9}$. In addition, Rubinstein and co-workers have developed scaling relationships for the polymer concentration inside of globules of collapsed diblock polyelectrolytes,^{50,52} finding that the concentration inside the globule should scale as $C \propto (l_B f)^{(3\nu - 1)/(2 - \nu)} \propto E^{-0.541}$, where the last proportionality substituted in for $\nu \approx 0.588$ for the good solvent case studied here. This scaling captures most of our data plotted in Fig. 4(a); however, it is clear from the data in Fig. 4(a) that we do not have simple power-law scaling between C and E . The scaling exponent is higher for small values of E and decreases as E becomes larger.

C. Comparison with RPA

Generally speaking, RPA does a good job of describing the symmetric systems that we have considered here.

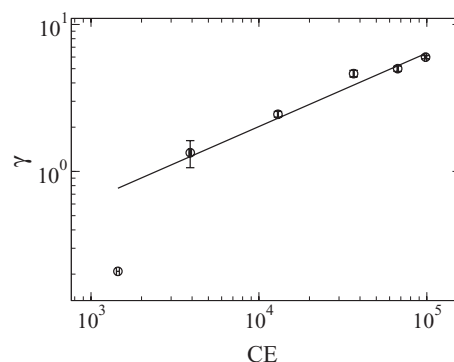


FIG. 7. Scaling of the interfacial tension in the absence of salt with the product CE , where C is the concentration of the polyelectrolytes in the coacervate phase. The solid line represents $\gamma \propto (CE)^{1/2}$. These data are taken from the simulations that are summarized in Fig. 4 where B was held constant and E was systematically varied.

The RPA binodal and spinodal phase boundaries are included above in Figures 4(a) and 5(a). As the dimensionless Bjerrum length E is reduced, the difference between RPA and the CL predictions of the phase boundary grows slightly, although RPA does a reliable job of qualitatively capturing the coexistence. The trends of the polymer concentration in the coacervate phase as the excluded volume parameter B is changed agree very well, although the agreement is not quantitative. The difference between the RPA phase boundary and the one predicted from CL simulations is relatively small and constant over the range of B investigated. In addition, the strong segregation predicted here where the polymer concentration is exceptionally small in the solvent-rich phase has also been predicted from RPA in θ -solvent conditions.⁵³

V. SUMMARY

In this work we have further developed a field-theoretic model that exhibits complex coacervation. The model was evaluated by numerically sampling the fully-fluctuating field theory, and we compared our results in some cases to the random-phase approximation. Following the work of Wang,²⁷ we also demonstrated a regularization procedure for our model such that it is free of ultraviolet divergences, and we have developed two methods for calculating the interfacial energy from a full field-theoretic simulation. The first method relies on the mechanical interpretation of the interfacial tension and examines the pressure differences in the plane of the interface compared to normal to the interface, while the second method estimates the change in free energy after the interfacial area is changed by a small amount. We believe these to be the first calculations of the interfacial tension in a field-theoretic simulation, and we explored the scaling relationships between the interfacial tension and various parameters of the model relating to electrostatic strength, salt concentration, and solvent quality.

ACKNOWLEDGMENTS

This work was partially supported by the MRSEC Program of the National Science Foundation under Award No.

DMR05-20415 and the Institute for Collaborative Biotechnologies through Grant No. W911NF-09-D-0001 from the U.S. Army Research Office. The content of the information does not necessarily reflect the position or the policy of the Government, and no official endorsement should be inferred.

APPENDIX A: DERIVATIVE OF \mathcal{H} WITH RESPECT TO BOX DIMENSIONS

In this Appendix we derive the expressions for the derivative of the Hamiltonian $\mathcal{H}[w, \psi]$ with respect to the box dimensions. First, we re-write our partition function \mathcal{Z} and the interaction potentials in scaled coordinates to isolate the dependence on the box dimensions

$$\mathcal{Z} = \frac{z_0 V^{n_T}}{n_+! n_-! n_{s+}! n_{s-}!} \int \mathcal{D}\mathbf{x}(s)^{n_+ + n_-} \times \int d\mathbf{x}^{n_T} \exp[-\beta U_0 - \beta U_1 - \beta U_2], \quad (\text{A1})$$

$$\beta U_0 = \frac{1}{4} \sum_{j=1}^{n_{\pm}} \int_0^1 ds \left(\frac{d\mathbf{x}_j(s)}{ds} \right) \cdot \mathbf{G} \cdot \left(\frac{d\mathbf{x}_j(s)}{ds} \right), \quad (\text{A2})$$

$$\beta U_1 = \frac{u_0}{2V} \int d\mathbf{x} [\hat{\rho}_P(\mathbf{x})]^2, \quad (\text{A3})$$

$$\beta U_2 = \frac{1}{2V} \int d\mathbf{x} \int d\mathbf{x}' \hat{\rho}_c(\mathbf{x}) \frac{l_B}{|\mathbf{h} \cdot (\mathbf{x} - \mathbf{x}')|} \hat{\rho}_c(\mathbf{x}'). \quad (\text{A4})$$

Tracing through the Hubbard-Stratonovich transformation leads to the Hamiltonian in scaled coordinates given by

$$\begin{aligned} H[w, \psi] = & \frac{V}{2B} \int d\mathbf{x} w(\mathbf{x})^2 + \frac{V}{2E} \\ & \times \int d\mathbf{x} [\mathbf{h}^{-1} \cdot \nabla_x \psi(\mathbf{x})] \cdot [\mathbf{h}^{-1} \cdot \nabla_x \psi(\mathbf{x})] \\ & - C_+ V \ln Q_+[\omega_+] - C_- V \ln Q_-[\omega_-] \\ & - C_{s+} V \ln Q_{s+} \left[\frac{iZ_{s+}}{ZN} \Gamma * \psi \right] \\ & - C_{s-} V \ln Q_{s-} \left[\frac{iZ_{s-}}{ZN} \Gamma * \psi \right]. \end{aligned} \quad (\text{A5})$$

Here, \mathbf{h} is the tensor that describes the shape of the simulation box, and for rectangular simulation boxes $h_{\alpha\beta} = L_\alpha \delta_{\alpha\beta}$, where α is one of the Cartesian directions and L_α is the length of the simulation box in the α -direction.²⁹ The scaled coordinates $\mathbf{x} = \mathbf{h}^{-1} \cdot \mathbf{r}$ represent the positions of ions and polymer segments scaled such that $x_\alpha \in [0:1]$. The derivatives of the terms involving the fields $w(\mathbf{x})$ and $\psi(\mathbf{x})$ are straightforward, and the derivatives of the polymer partition functions Q_\pm and the small-ion partition functions $Q_{s\pm}$ are detailed below. The Gaussian smearing functions in scaled coordinates are given by

$$\Gamma(\mathbf{r} - \mathbf{r}') = \left(\frac{1}{2\pi^2 a^2} \right)^{3/2} e^{-(\mathbf{x} - \mathbf{x}') \cdot \mathbf{G} \cdot (\mathbf{x} - \mathbf{x}') / 2a^2}. \quad (\text{A6})$$

In Eq. (A6), we have isolated the dependence of $\Gamma(\mathbf{r})$ on the box dimensions by writing the dot product in terms of the metric tensor \mathbf{G} , which is defined as $\mathbf{G} = \mathbf{h}^T \mathbf{h}$ and \mathbf{h} is the tensor that describes the shape of the simulation box.

The derivative of the polymer partition functions closely follows that detailed in Appendix A of Ref. 54. In scaled coordinates, the single-chain partition functions are given by

$$Q_\pm[\omega_\pm] = \frac{\int \mathcal{D}\mathbf{x}(s) \exp[-\beta U_0 - \int_0^1 ds \omega_\pm(\mathbf{x})]}{\int \mathcal{D}\mathbf{x}(s) \exp(-\beta U_0)}, \quad (\text{A7})$$

where $\omega_\pm(\mathbf{x})$ is given by Eq. (10). The path integrals over the chain contours in Eq. (A7) can be discretized as $N_s + 1$ integrals over particle positions with N_s discrete bonds separating them to yield

$$\begin{aligned} Q_\pm[\omega_\pm] = & \int d\mathbf{x}^{N_s+1} e^{-\Delta s \omega_\pm(\mathbf{x}_{N_s})} \\ & \times \Phi(\mathbf{x}_{N_s} - \mathbf{x}_{N_s-1}) e^{-\Delta s \omega_\pm(\mathbf{x}_{N_s-1})} \\ & \times \Phi(\mathbf{x}_{N_s-1} - \mathbf{x}_{N_s-2}) \dots e^{-\Delta s \omega_\pm(\mathbf{x}_1)} \\ & \times \Phi(\mathbf{x}_1 - \mathbf{x}_0) e^{-\Delta s \omega_\pm(\mathbf{x}_0)}. \end{aligned} \quad (\text{A8})$$

The function $\Phi(\mathbf{x}_i - \mathbf{x}_{i-1})$ is the normalized bond transition probability for a Gaussian chain and is given by

$$\begin{aligned} \Phi(\mathbf{x}_i - \mathbf{x}_{i-1}) = & \left(\frac{1}{\pi \Delta s} \right)^{3/2} \exp \left[-\frac{1}{\Delta s} \sum_{\alpha, \beta} (x_{i, \alpha} - x_{i-1, \alpha}) \right. \\ & \times G_{\alpha\beta} (x_{i, \beta} - x_{i-1, \beta}) \left. \right]. \end{aligned} \quad (\text{A9})$$

The derivatives of $Q_\pm[\omega_\pm]$ with respect to the box dimensions yield two terms that contribute to $\frac{\partial \mathcal{H}}{\partial L_\alpha}$: the first arises from the derivative of $\Phi(\mathbf{x}_i - \mathbf{x}_{i-1})$ and is detailed in Ref. 54, and the second arises from the derivative of the convolution of the fields with the Gaussian “smearing” functions ($\frac{\partial \Gamma}{\partial L_\alpha}$). Recalling that $\omega_\pm(\mathbf{r}) = (\Gamma * w_\pm)(\mathbf{r})$ convolution of Γ with the fields given in Eq. (10) can be discretized and written in Fourier space as

$$\omega_\pm(\mathbf{x}) = \frac{i}{N} \sum_{\mathbf{k}} e^{i\mathbf{k} \cdot \mathbf{x}} \exp \left[-\frac{a^2}{2} \sum_{\alpha, \beta} k_\alpha G_{\alpha\beta}^{-1} k_\beta \right] \hat{w}_\pm(\mathbf{k}), \quad (\text{A10})$$

where the hats indicate Fourier transformed functions. Restricting ourselves to purely rectangular boxes ($G_{\alpha\beta} = 0$ for $\alpha \neq \beta$) and taking the derivative of $\omega_\pm(\mathbf{x})$ leads to

$$\begin{aligned} \frac{\partial \omega_\pm(\mathbf{x})}{\partial L_\alpha} = & -\frac{ia^2}{NL_\alpha} \sum_{\mathbf{k}} e^{i\mathbf{k} \cdot \mathbf{x}} \\ & \times \exp \left[-\frac{a^2}{2} \sum_{\alpha, \beta} k_\alpha G_{\alpha\beta}^{-1} k_\beta \right] k_\alpha^2 \hat{w}_\pm(\mathbf{k}), \end{aligned} \quad (\text{A11})$$

$$= \frac{ia^2}{NL_\alpha^3} (\Gamma * \nabla_{x, \alpha}^2 w_\pm)(\mathbf{x}). \quad (\text{A12})$$

Inserting this expression for the derivative of $\omega_{\pm}(\mathbf{x})$ and the expression from Ref. 54 for the terms that arise from the derivatives of $\Phi(\mathbf{x}_i - \mathbf{x}_{i-1})$, we arrive at

$$\begin{aligned} \frac{\partial Q_{\pm}[\omega_{\pm}]}{\partial L_{\alpha}} = & \sum_{n=0}^{N_s} \left[\int d\mathbf{x}^{N_s+1} \prod_{i=0}^{n-1} e^{-\Delta s \omega_{\pm}(\mathbf{x}_{N_s-i})} \right. \\ & \times \Phi(\mathbf{x}_{N_s-i} - \mathbf{x}_{N_s-i-1}) \\ & \times e^{-\Delta s \omega_{\pm}(\mathbf{x}_{N_s-n})} \left(-\frac{2\Delta s}{L_{\alpha}^3} \right) \\ & \times \nabla_{x_{\alpha}}^2 \Phi(\mathbf{x}_{N_s-n} - \mathbf{x}_{N_s-n-1}) e^{\Delta s \omega_{\pm}(\mathbf{x}_{N_s-n-1})} \\ & \times \prod_{j=n+1}^{N_s-1} \Phi(\mathbf{x}_{N_s-j} - \mathbf{x}_{N_s-j-1}) e^{-\Delta s \omega_{\pm}(\mathbf{x}_{N_s-j-1})} \left. \right] \\ & + \sum_{j=1}^{N_s} \left[\int d\mathbf{x}^{N_s+1} \prod_{i=0}^{j-1} e^{-\Delta s \omega_{\pm}(\mathbf{x}_{N_s-i})} \right. \\ & \times \Phi(\mathbf{x}_{N_s-i} - \mathbf{x}_{N_s-i-1}) \\ & \times e^{-\Delta s \omega_{\pm}(\mathbf{x}_{N_s-j})} \left\{ -\Delta s \left(\frac{\partial \omega_{\pm}}{\partial L_{\alpha}} \right) \right\} \\ & \times \Phi(\mathbf{x}_{N_s-j} - \mathbf{x}_{N_s-j-1}) \\ & \times \prod_{i=j+1}^{N_s} e^{-\Delta s \omega_{\pm}(\mathbf{x}_{N_s-i})} \Phi(\mathbf{x}_{N_s-i} - \mathbf{x}_{N_s-i-1}) \left. \right]. \end{aligned} \quad (\text{A13})$$

Inserting Eq. (A12) and restoring the continuum limit leads to

$$\begin{aligned} \frac{\partial Q_{\pm}[\omega_{\pm}]}{\partial L_{\alpha}} = & -\frac{2}{L_{\alpha}^3} \int d\mathbf{x} \int ds q_{\pm}(\mathbf{x}, s; [\omega_{\pm}]) \\ & \times \nabla_{x_{\alpha}}^2 q^{\dagger}(\mathbf{x}, 1-s; [\omega_{\pm}]) \\ & - \frac{ia^2}{NL_{\alpha}^3} \int d\mathbf{x} \int ds q(\mathbf{x}, s; [\omega_{\pm}]) \\ & \times q^{\dagger}(\mathbf{x}, 1-s; [\omega_{\pm}]) (\Gamma * \nabla_{x_{\alpha}}^2 w_{\pm})(\mathbf{x}), \end{aligned} \quad (\text{A14})$$

$$\begin{aligned} = & -\frac{2}{L_{\alpha}^3} \int d\mathbf{x} \int ds q_{\pm}(\mathbf{x}, s; [\omega_{\pm}]) \\ & \times \nabla_{x_{\alpha}}^2 q^{\dagger}(\mathbf{x}, 1-s; [\omega_{\pm}]) \\ & - \frac{ia^2 Q_{\pm}[\omega_{\pm}]}{Nn_{\pm} L_{\alpha}^3} \int d\mathbf{x} \tilde{\rho}_{\pm}(\mathbf{x}; [\omega_{\pm}]) \\ & \times (\Gamma * \nabla_{x_{\alpha}}^2 w_{\pm})(\mathbf{x}). \end{aligned} \quad (\text{A15})$$

where the definition of the density operator has been inserted into Eq. (A15). Reverting to the unscaled (\mathbf{r}) coordinates yields the appropriate terms in Eq. (20) above.

The final contributions to the derivative of \mathcal{H} arise from the derivatives of the small ion partition functions $Q_{s\pm}$ given in Eq. (16). Similar to the result for the derivative of the polymer partition function, there is a contribution to this derivative arising from the derivative of $\Gamma(\mathbf{r} - \mathbf{r}')$. Tracing the same steps for the small-ion partition function leads to the final

result

$$\frac{\partial Q_{s\pm}}{\partial L_{\alpha}} = \frac{iZ_{s\pm}V}{ZNL_{\alpha}} \int d\mathbf{x} \tilde{\rho}_{s\pm}(\mathbf{x}) (\Gamma * \psi)(\mathbf{x}). \quad (\text{A16})$$

APPENDIX B: BENNETT'S FREE ENERGY DIFFERENCE METHOD

Bennett's method begins by noting that the free energy difference between two states 0 and 1 can be trivially expressed as a ratio of two partition functions as

$$\beta \Delta F_{10} = \beta(F_1 - F_0) = \ln \frac{Z_0}{Z_1}. \quad (\text{B1})$$

Here, we will employ a generic field-theoretic partition function

$$Z_0 = z_0 \int \mathcal{D}w e^{-\mathcal{H}[w]}, \quad (\text{B2})$$

where z_0 contains all of the prefactors, including the thermal de Broglie wavelengths, factors of $1/n!$, and the numerical pre-factors that arise from the Gaussian integrals employed in the Hubbard-Stratonovich transformation. The ratio of partition functions in Eq. (B1) can be re-written as

$$\frac{Z_0}{Z_1} = \frac{Z_0 \int \mathcal{D}w W \exp(-H_0 - H_1)}{Z_1 \int \mathcal{D}w W \exp(-H_0 - H_1)} = \frac{\langle W \exp(-H_0) \rangle_1}{\langle W \exp(-H_1) \rangle_0}, \quad (\text{B3})$$

where the angular brackets $\langle \dots \rangle_0$ denote averages in the canonical ensemble following the Hamiltonian \mathcal{H}_0 (or \mathcal{H}_1 for $\langle \dots \rangle_1$), and W is an unspecified weighting function. It is important to note that the configuration space covered by the functional integrals $\int \mathcal{D}w$ in Eq. (B3) must be the same for state 0 and 1. Since the two states of interest when calculating the interfacial tension are states of equal volume but different shapes, this requirement can be satisfied by writing the partition function in scaled coordinates as done in Appendix A. The prefactors of volume will cancel since the volume is equal in the two states, thus giving a numerical estimate of ΔF as the interfacial area is changed by $\Delta A = A_1 - A_0$. This method can be used for a generic free energy difference; in our case, the two states 0 and 1 are two states with different interfacial areas between the coacervate and the supernatant but with the same total system volume.

The next step in Bennett's approach is to determine the form of the weighting function, W . One assumes that the error in the estimate of the free energy change obeys Gaussian statistics and minimizes the error $(\Delta F_{est} - \Delta F)^2$. This leads to the working equation of Bennett's method,⁵⁵

$$\frac{Z_0}{Z_1} = \frac{\langle f(\mathcal{H}_0 - \mathcal{H}_1 + C) \rangle_1}{\langle f(\mathcal{H}_1 - \mathcal{H}_0 - C) \rangle_0} \exp(C) \quad (\text{B4})$$

$$= \frac{\langle f(\Delta \mathcal{H}_{01} + C) \rangle_1}{\langle f(\Delta \mathcal{H}_{10} - C) \rangle_0} \exp(C), \quad (\text{B5})$$

where $\Delta \mathcal{H}_{ij} = \mathcal{H}_i - \mathcal{H}_j$, and $f(x) = [1 + \exp(x)]^{-1}$ is the Fermi function. The optimal value of C satisfies the equation

$$\langle f(\Delta \mathcal{H}_{01} + C) \rangle_1 = \langle f(\Delta \mathcal{H}_{10} - C) \rangle_0. \quad (\text{B6})$$

To solve for C in Eq. (B6), one must first obtain sufficient statistics on $\Delta\mathcal{H}_{01}$ when sampling according to \mathcal{H}_1 and $\Delta\mathcal{H}_{10}$ when sampling according to \mathcal{H}_0 . These changes in \mathcal{H} are obtained by occasionally perturbing into the second state and calculating the change in \mathcal{H} . In the present case where we are interested in calculating the interfacial tension, the two states 0 and 1 correspond to states with the same volume but different interfacial areas between the coacervate and the solvent, A_0 and A_1 . To calculate $\Delta\mathcal{H}_{01}$ when sampling according to \mathcal{H}_1 , we occasionally scale our simulation box so that it has the same shape as the system sampling according to \mathcal{H}_0 , calculate the new value of \mathcal{H} to get $\Delta\mathcal{H}_{01}$, then return to the original A_1 box shape and resume our simulation.

It is important to note that the configuration space covered by the functional integrals $\int \mathcal{D}w$ in Eq. (B3) must be the same for state 0 and 1. Since the two states of interest when calculating the interfacial tension are states of equal volume but different shapes, this requirement can be satisfied by writing the partition function in scaled coordinates as done in Appendix A. The prefactors of volume will cancel since the volume is equal in the two states, thus giving a numerical estimate of ΔF as the interfacial area is changed by $\Delta A = A_1 - A_0$.

- ¹J. Schlenoff and S. Dubas, *Macromolecules* **34**, 592 (2001).
- ²G. Decher, *Science* **277**, 1232 (1997).
- ³M. E. Davis, *Mol. Pharmaceut.* **6**, 659 (2009).
- ⁴H. Zhao, C. Sun, R. Stewart, and J. Waite, *J. Biol. Chem.* **280**, 42938 (2005).
- ⁵R. Kausik, A. Srivastava, P. Korevaar, G. Stucky, J. Waite, and S. Han, *Macromolecules* **42**, 7404 (2009).
- ⁶H. Shao, K. Bachus, and R. Stewart, *Macromol. Biosci.* **9**, 464 (2009).
- ⁷R. Stewart, C. Wang, and H. Shao, *Adv. Colloid Interface Sci.* **167**, 85 (2011).
- ⁸L. Luzzi, *J. Pharm. Sci.* **59**, 1367 (1970).
- ⁹A. Ohsugi, H. Furukawa, A. Kakugo, Y. Osada, and J. Gong, *Macromol. Rapid Commun.* **27**, 1242 (2006).
- ¹⁰I. Voets, A. de Keizer, and M. Cohen Stuart, *Adv. Colloid Interface Sci.* **147**, 300 (2009).
- ¹¹H. Shao and R. Stewart, *Adv. Mater.* **22**, 729 (2010).
- ¹²C. Jewell and D. Lynn, *Adv. Drug Delivery Rev.* **60**, 979 (2008).
- ¹³E. Spruijt, J. Sprakel, M. Cohen-Stuart, and J. van der Gucht, *Soft Matter* **6**, 172 (2009).
- ¹⁴V. Borue and I. Erukhimovich, *Macromolecules* **23**, 3625 (1990).
- ¹⁵V. Boryu and I. Erukhimovich, *Macromolecules* **21**, 3240 (1988).
- ¹⁶M. Castelnovo and J. Joanny, *Eur. Phys. J. E* **6**, 377 (2001).
- ¹⁷A. Kudlay and M. de la Cruz, *J. Chem. Phys.* **120**, 404 (2004).
- ¹⁸A. Kudlay, A. Ermoshkin, and M. De La Cruz, *Macromolecules* **37**, 9231 (2004).
- ¹⁹R. Kumar, D. Audus, and G. Fredrickson, *J. Phys. Chem. B* **114**, 9956 (2010).
- ²⁰G. Fredrickson, V. Ganesan, and F. Drolet, *Macromolecules* **35**, 16 (2002).
- ²¹E. M. Lennon, G. O. Mohler, H. D. Cenicerros, C. J. García-Cervera, and G. H. Fredrickson, *Multiscale Model. Simul.* **6**, 1347 (2008).
- ²²J. Lee, Y. O. Popov, and G. H. Fredrickson, *J. Chem. Phys.* **128**, 224908 (2008).
- ²³Y. O. Popov, J. Lee, and G. H. Fredrickson, *J. Polym. Sci., Part B: Polym. Phys.* **45**, 3223 (2007).
- ²⁴F. J. Solis and M. O. de la Cruz, *J. Chem. Phys.* **112**, 2030 (2000).
- ²⁵M. Muthukumar, J. Hua, and A. Kundagrami, *J. Chem. Phys.* **132**, 084901 (2010).
- ²⁶A. Alexander-Katz, A. G. Moreira, S. W. Sides, and G. H. Fredrickson, *J. Chem. Phys.* **122**, 014904 (2005).
- ²⁷Z.-G. Wang, *Phys. Rev. E* **81**, 021501 (2010).
- ²⁸G. H. Fredrickson, *The Equilibrium Theory of Inhomogeneous Polymers* (Oxford University Press, New York, 2006).
- ²⁹M. Parrinello and A. Rahman, *J. Chem. Phys.* **76**, 2662 (1982).
- ³⁰M. Parrinello and A. Rahman, *J. Appl. Phys.* **52**, 7182 (1981).
- ³¹J. S. Rowlinson and B. Widom, *Molecular Theory of Capillarity* (Oxford University Press, New York, 1982).
- ³²M. Zhou, *Proc. R. Soc. London, Ser. A* **459**, 2347 (2003).
- ³³M. Zhou, *Proc. R. Soc. London, Ser. A* **461**, 3437 (2005).
- ³⁴G. C. Rossi and M. Testa, *J. Chem. Phys.* **132**, 074902 (2010).
- ³⁵F. Varnik, J. Baschnagel, and K. Binder, *Phys. Rev. E* **65**, 021507 (2002).
- ³⁶J. Alejandre, D. J. Tildesley, and G. A. Chapela, *J. Chem. Phys.* **102**, 4574 (1995).
- ³⁷G. Gloor, G. Jackson, F. Blas, and E. de Miguel, *J. Chem. Phys.* **123**, 134703 (2005).
- ³⁸J. R. Errington and D. A. Kofke, *J. Chem. Phys.* **127**, 174709 (2007).
- ³⁹E. Lennon, K. Katsov, and G. Fredrickson, *Phys. Rev. Lett.* **101**, 138302 (2008).
- ⁴⁰C. H. Bennett, *J. Comput. Phys.* **22**, 245 (1976).
- ⁴¹E. Salomons and M. Mareschal, *J. Phys. Condens. Matter* **3**, 3645 (1991).
- ⁴²K. O. Rasmussen and G. Kalosakas, *J. Polym. Sci., Part B: Polym. Phys.* **40**, 1777 (2002).
- ⁴³G. Tzeremes, K. O. Rasmussen, T. Lookman, and A. Saxena, *Phys. Rev. E* **65**, 041806 (2002).
- ⁴⁴G. Parisi, *Phys. Lett. B* **131**, 393 (1983).
- ⁴⁵J. R. Klauder, *Journal of Physics A: Mathematical and Theoretical* **16**, L317 (1983).
- ⁴⁶M. Villet and G. Fredrickson, *J. Chem. Phys.* **132**, 034109 (2010).
- ⁴⁷G. Jones and W. Ray, *J. Am. Chem. Soc.* **59**, 187 (1937).
- ⁴⁸P. Petersen, J. Johnson, K. Knutsen, and R. Saykally, *Chem. Phys. Lett.* **397**, 46 (2004).
- ⁴⁹R. Wang and Z.-G. Wang, *J. Chem. Phys.* **135**, 014707 (2011).
- ⁵⁰N. Shusharina, E. Zhulina, A. Dobrynin, and M. Rubinstein, *Macromolecules* **38**, 8870 (2005).
- ⁵¹N. Oskolkov and I. Potemkin, *Macromolecules* **40**, 8423 (2007).
- ⁵²Z. Wang and M. Rubinstein, *Macromolecules* **39**, 5897 (2006).
- ⁵³I. Potemkin and V. Palyulin, *Phys. Rev. E* **81**, 041802 (2010).
- ⁵⁴R. A. Riggleman and G. H. Fredrickson, *J. Chem. Phys.* **132**, 024104 (2010).
- ⁵⁵C. Bennett, *J. Comput. Phys.* **22**, 245 (1976).